Simulation and experimental verification of the diffusion in an anisotropic fiber phantom

Els Fieremans [a,*], Yves De Deene [b], Steven Delputte [a], Mahir S. Özdemir [a], Yves D'Asseler [a], Jelle Vlassenbroeck [c], Karel Deblaere [d], Eric Achten [d], Ignace Lemahieu [a]

[a] *Department of Electronics and Information Systems, MEDISIP, Ghent University-IBBT-IBiTech, De Pintelaan 185 block B, B-9000 Ghent, Belgium*
[b] *Department of Radiotherapy and Nuclear Medicine, Ghent University Hospital, De Pintelaan 185, B-9000 Ghent, Belgium*
[c] *Department of Subatomic and Radiation Physics, Ghent University, Proeftuinstraat 86, B-9000 Ghent, Belgium*
[d] *Department of Radiology, Ghent University Hospital, De Pintelaan 185, B-9000 Ghent, Belgium*

Abstract

Diffusion weighted magnetic resonance imaging enables the visualization of fibrous tissues such as brain white matter. The validation of this non-invasive technique requires phantoms with a well-known structure and diffusion behavior. This paper presents anisotropic diffusion phantoms consisting of parallel fibers. The diffusion properties of the fiber phantoms are measured using diffusion weighted magnetic resonance imaging and bulk NMR measurements. To enable quantitative evaluation of the measurements, the diffusion in the interstitial space between fibers is modeled using Monte Carlo simulations of random walkers. The time-dependent apparent diffusion coefficient and kurtosis, quantifying the deviation from a Gaussian diffusion profile, are simulated in 3D geometries of parallel fibers with varying packing geometries and packing densities. The simulated diffusion coefficients are compared to the theory of diffusion in porous media, showing a good agreement. Based on the correspondence between simulations and experimental measurements, the fiber phantoms are shown to be useful for the quantitative validation of diffusion imaging on clinical MRI-scanners.
© 2007 Elsevier Inc. All rights reserved.

Keywords: Diffusion; Fiber phantom; Porous media; Monte Carlo simulation; Random walk; Kurtosis

1. Introduction

Diffusion weighted magnetic resonance imaging (DW-MRI) provides a non-invasive tool to explore fibrous tissue *in vivo*. An interesting application for DW-MRI is the investigation of brain white matter where the insight in the anatomy of neuronal networks is of great interest for the understanding of normal and pathological processes affecting brain functions (for an overview see [1]). In order to develop an accurate quality assessment of DW-MRI on clinical MRI-scanners a hardware diffusion phantom with a well-known structure and diffusion behavior is required. The hardware diffusion phantom may serve as the ground-truth for the quantitative validation of the measurement of diffusion parameters, such as the apparent diffusion coefficient (D_{app}) and fractional anisotropy (FA).

Among the hardware diffusion phantoms described in the literature, isotropic liquids with a well established diffusion constant [2] are used in quality protocols [3]. Besides plants [4] and other biological phantoms [5,6], several non-organic anisotropic hardware diffusion phantoms have been proposed recently: capillary phantoms [7–9] and fiber phantoms [10,11]. Both kinds of phantoms are intended for the validation and quality assessment of DW-MRI and Q-ball imaging on clinical MRI-scanners. However, to enable quantitative analysis, it is crucial to obtain an accurate description of the diffusion properties of these phantoms.

In this work, we present an anisotropic diffusion fiber phantom useful for the quantitative validation of

---

[*] Corresponding author. Fax: +32 92404159.
E-mail address: Els.Fieremans@ugent.be (E. Fieremans).

DW-MRI on clinical MRI-scanners. The fiber structure is investigated by obtaining a high-resolution computer tomography (CT) scan and its time-dependent diffusion properties are measured using DW-MRI and bulk NMR measurements.

To enable quantitative evaluation of the measurements, the diffusion is modeled in the interstitial space of the fiber phantom by Monte Carlo simulations of random walkers. Numerical results are presented for hindered diffusion in the interstitial space between fibers by modeling the diffusion coefficient, characterizing the Gaussian diffusion profile, and the excess kurtosis, which is a measure of the deviation from a Gaussian diffusion profile. The influence of the fiber packing density and ordered versus random packing geometry on the diffusion behavior is examined from the short-time to the long-time diffusion limit. Hence, a framework is created by which the diffusion parameters can be estimated based on the phantom characteristics and diffusion time.

The anisotropic fiber phantom constructed for this study can be regarded as a two-dimensional (2D) porous medium. Therefore, simulation results can be compared to the analytical equations derived for diffusion in porous media. The validation of these theoretical models has already been demonstrated for porous media in three dimensions with random packed beads [12,13] and various types of porous rocks [14,15]. In this paper, we compare the simulation and experimental results with the analytical model for diffusion within porous media in two dimensions.

Theoretical models for diffusion in porous media have been applied to model the time-dependent diffusion in biological systems, such as brain white matter [16–18]. The diffusion behavior within the constructed fiber phantoms is in accordance with a model for the diffusion in the extracellular space of brain white matter [19]. As the origin of the DW-MRI signal remains in general unclear, the simulations provided here may also serve as a tool to systematically study the link between the apparent diffusion properties and the underlying structure of brain white matter.

2. Theory

The diffusion of water can be seen as a random process and hence the displacement of a water molecule can be described by a probability function. For free diffusion in homogeneous media, this displacement probability function is a Gaussian function with a characteristic width proportional to the diffusion coefficient D_{free}. However for long diffusion times in heterogeneous tissue, the diffusion becomes anisotropic and is described by the apparent diffusion coefficient D_{app} or the diffusivity for a given direction $\vec{n}$, defined by:

$$D_{app}(\Delta) = \frac{1}{2\Delta}\langle(\vec{n}.\vec{s})^2\rangle \tag{1}$$

where $\vec{s}$ is the net displacement of a particle during a diffusion time Δ.

An additional metric to characterize the diffusion in heterogeneous media is the apparent excess diffusion kurtosis K_{app}, quantifying the deviation from a Gaussian diffusion profile, defined by:

$$K(\Delta) = \frac{\langle(\vec{n}.\vec{s})^4\rangle}{\langle(\vec{n}.\vec{s})^2\rangle^2} - 3 \tag{2}$$

The excess diffusion kurtosis, also called "diffusion kurtosis", equals zero in case of a Gaussian diffusion profile and becomes negative if the diffusion profile is more sharply peaked than a Gaussian distribution and positive if the diffusion profile is less sharply peaked.

Both parameters D_{app} and K_{app} can be determined for a given diffusion time Δ with a standard diffusion weighted Stejskal–Tanner sequence [20] with varying narrow gradients g, by fitting the obtained signal $\ln\left(\frac{S(b)}{S(b=0)}\right)$ to the key relationship defined in [21]:

$$\ln\left(\frac{S(b)}{S(b=0)}\right) = -bD_{app} + \frac{1}{6}b^2 D_{app}^2 K_{app} + O(b^3) \tag{3}$$

where $S(b)$ is the signal intensity at the echo time and b is given by the usual expression $b = (\gamma\delta g)^2(\Delta - \delta/3)$ [22], where γ is the proton gyro magnetic ratio and δ is the duration of the gradient with strength g.

The fiber phantoms in this study can be modeled as a porous medium with a matrix consisting of an infinite pack of cylinders. The properties of D_{app} are reasonably well understood in porous media, i.e., media consisting of an impermeable matrix filled with an MR-visible fluid.

In the case of diffusion at short times, the mean diffusion length $l_d = \sqrt{D_{free}\Delta}$ remains smaller than the typical pore size so that only the molecules located in a layer with a thickness of the order l_d can sense the presence of the surface [23,24,12]. This implies that the diffusion behavior is determined by the surface-to-volume ratio S/V, with V the volume of the fluid. When the effects of spin relaxation at the boundaries are negligible, the time course of D_{app} as a function of diffusion time in the direction perpendicular to the infinitely long cylinders is dependent on the cylinder density and the cylinder diameter according to the following equation [23]:

$$\frac{D_{app}(\Delta)}{D_{free}} = 1 - \frac{2}{3\sqrt{\pi}}\frac{S}{V}\sqrt{D_{free}\Delta} + O(D_{free}\Delta) \tag{4}$$

In the opposite limiting case of long diffusion times, the molecules can travel distances much longer than the pore size. The diffusion coefficient becomes constant and can be described by the following formula, introducing the tortuosity parameter λ [12].

$$\frac{D_{app}(\Delta)}{D_{free}} = \frac{1}{\lambda} + \frac{\mu_1}{\Delta} + \frac{\mu_2}{\Delta^{3/2}} \tag{5}$$

where μ_1 and μ_2 are constants depending on the details of the geometry. The tortuosity is a property of the medium,

i.e., the geometry and the connectivity of the pores. In general, its relation with the medium is not very clear. The tortuosity has been theoretically predicted in [18], where the Maxwell–Garnett equations [25] are applied to diffusion in a lattice consisting of regular arrays of square and hexagonally packed cylinders. The formulas derived in [18] for hollow cylinders with a given thickness can be simplified to the situation described here with no water molecules inside the cylinders.

The following formula, based on a 2-point Padé approximation, has been widely used to interpolate between the short-time and the long-time limit [12,13,26]:

$$\frac{D_{app}(\Delta)}{D_{free}}$$
$$= 1 - \left(1 - \frac{1}{\lambda}\right) \frac{\frac{2}{3\sqrt{\pi}} \frac{S}{V}\sqrt{D_{free}\Delta} + \left(1 - \frac{1}{\lambda}\right)\frac{D_{free}\Delta}{D_{free}\theta}}{\left(1 - \frac{1}{\lambda}\right) + \frac{2}{3\sqrt{\pi}} \frac{S}{V}\sqrt{D_{free}\Delta} + \left(1 - \frac{1}{\lambda}\right)\frac{D_{free}\Delta}{D_{free}\theta}}$$

(6)

with θ a time constant defining the Padé length$= \sqrt{D_{free}\theta}$. This is the length scale during which the diffusion process of a particle converts from the short diffusion time limit to the long diffusion time.

In this paper, we used Monte Carlo simulations of $D_{app}(\Delta)$ to verify the theory of diffusion in the case of ordered and random 2D fiber geometries. In particular, the correspondence with Archie's law was investigated and the Padé approximant, interpolating the diffusion coefficient in the intermediate time between short- and long-time diffusion limit, was fitted to the simulation results.

3. Materials and methods

3.1. Monte Carlo simulations

Random water molecule displacement was simulated in Matlab by a three-dimensional Monte Carlo simulation of random walkers. For each simulation, 100,000 particles were initially randomly spread in a square plane of 1 mm × 1 mm, which was oriented transverse in a packing of infinitely long parallel aligned impermeable rigid cylinders. The trajectory of one spin particle was generated by moving the particle during each time step t over a distance of $\sqrt{6D_{free}t}$ (with D_{free} the diffusion coefficient of water in a free medium) in a randomly chosen radial direction. The random direction was selected using spherical coordinates by choosing the radial coordinate r, the azimuthal angle θ and the polar angle ϕ according to:

$$r = \sqrt{6D_{free}t}$$
$$\theta = 2\pi u$$
$$\phi = \arccos(1 - 2v)$$

with u and v numbers generated uniform randomly between 0 and 1. At the cylinder boundaries, particles were elastically reflected. In the direction along the cylinders, the particles can travel infinitely long. In the transverse

direction, random walkers that reach one side of the 1 mm × 1 mm square, re-enter again at the opposite side of the square. The packing geometries of cylinders are defined such that a continuous geometry is obtained when repeating the square periodically in two dimensions. For each random walker, the number of times that it leaves and enters the square at each side is recorded so that for a given diffusion time Δ, the total traveled distance could be calculated correctly. The first and higher order moments of the total traveled distance in the x-, y- and z-direction are used to calculate the apparent diffusion coefficient D_{app} and the apparent diffusion kurtosis K_{app} according to the corresponding definitions, Eqs. (1) and (2).

The accuracy of the simulation results is assessed by determining the accuracy of the diffusion coefficient and kurtosis in the z-direction. Since the diffusion is not restricted in this direction, the diffusion coefficient should equal the diffusion coefficient of a free medium D_{free} and the kurtosis should be zero. Averages of the diffusion coefficient in the z-direction were taken over the simulated time range for each fiber density. For each fiber geometry, the relative deviation of the mean value of those averages from D_{free} was calculated as a measure for accuracy. The standard deviation of the diffusion coefficient and kurtosis over time was taken as a measure of the precision of the simulations. A step length of 1.6 μm (thus a time step of 0.23 ms) was chosen because the differences between the current simulation results and the simulation results obtained with a much smaller step length (0.5 μm) were within the precision of the simulation. Given the fact that the simulation time increases quadratically with decreasing step length, this step length was considered as a fair compromise.

Simulations were performed for a hexagonal, square and random packing of parallel aligned cylinders (see Fig. 1) at a temperature of 20 °C ($D_{free} = 2.023 \times 10^{-3}$ mm²/s [2]) and for a free diffusion length $l_d = \sqrt{D_{free}\Delta}$ (with Δ the diffusion observation time) of 50 μm. Increasing fiber densities (from 0.02 up to the closest possible packing) were considered.

Ordered packing geometries with varying fiber density (FD = 0.02, 0.06,...) were obtained by generating hexagonal and square grids whereby the distance between neighboring grid points, representing the center point of the cylinders, was narrowed down to the densest packing (0.91 for a hexagonal and 0.785 for a square packing). For these simulations, the cylinders had a fixed diameter of 20 μm.
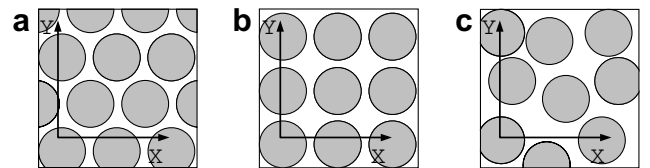

Fig. 1. The different types of fiber packing geometries and the corresponding coordinate axes used in the Monte Carlo simulations: (a) hexagonal, (b) square, (c) random.

Random packings were produced by Monte Carlo generation of a given number of circles in a square (1 mm × 1 mm), whereby the cylinders were not allowed to overlap. The effect of the variation of fiber radius was investigated by generating random packing geometries containing cylinders with a fixed diameter of 20 μm and comparing these simulation results with those obtained in random packing geometries containing cylinders with a Gaussian distributed diameter of 20 ± 4.1 μm (standard deviation). The effect of the packing density was examined by increasing the density in steps of 0.04 starting from 0.02 up to the highest feasible densities reproduced with the program, i.e., 0.54 for the simulations with a fixed diameter and 0.7 for the simulations with a variable diameter.

In the case of a packing geometry of infinitely long parallel packed cylinders, we expect that the principal frame of reference of the diffusion tensor coincides with the axes of a coordinate system chosen according to the three orthogonal directions x, y and z with the z-direction parallel to the cylinders. This hypothesis is confirmed in [18,27] and experimentally verified by the simulation results, showing that the diffusive motions parallel and perpendicular to the cylinders are statistically independent and that the diffusion coefficient is the same in all directions perpendicular to the cylinders. The apparent diffusion coefficients in the x-, y- and z-direction are thus the eigenvalues of the diffusion tensor. The diffusion tensor (DT) is then given by:

$$DT = \begin{pmatrix} D_{appZ} & 0 & 0 \\ 0 & D_{appX} & 0 \\ 0 & 0 & D_{appY} \end{pmatrix} \quad (7)$$

Fractional anisotropy (FA), characterizing the degree of diffusion anisotropy, was calculated using the following equation [28]:

$$FA = \frac{\sqrt{(D_{appZ} - D_{appX})^2 + (D_{appZ} - D_{appY})^2 + (D_{appX} - D_{appY})^2}}{\sqrt{2}\sqrt{D_{appZ}^2 + D_{appX}^2 + D_{appY}^2}} \quad (8)$$

3.2. Experiments

3.2.1. Fabrication process of the fiber phantoms

The diffusion fiber phantoms in this study were fabricated by holding Dyneema® fibers tightly together with a flexible, poly-olefin low-temperature shrinking tube (see Fig. 2). The Dyneema® wires were untwisted, uncoated and consisted each of 780 parallel aligned ultra-high-molecular-weight-poly-ethylene (UHMWPE) fiber filaments (diameter 20 μm, specifications provided by manufacturer), which are impermeable to water molecules and highly hydrophobic. To reduce the effect of susceptibility differences caused by air bubbles, the whole fabrication process was performed under water. Remaining air bubbles in the fiber phantoms were removed by squeezing and repetitively placing the phantoms in a vacuum chamber
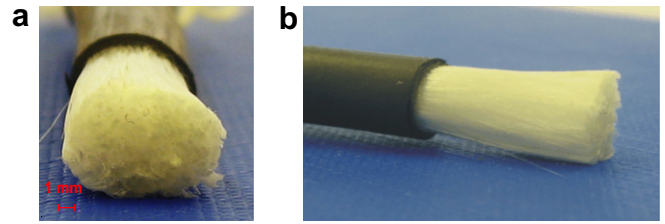

Fig. 2. Photographs of a fiber phantom with the shrinking tube partly removed: (a) transversal, (b) longitudinal view.

and subsequently in an ultrasonic bath to remove small bubbles attached to the fibers and the shrinking tube.

To determine the micro structure and the packing geometry, a fiber bundle phantom with an external diameter of 3 mm was manufactured and scanned with an X-ray micro-CT at an isotropic resolution of 3.4 μm. A directional X-ray tube was used, at a focal spot size of approximately 3.5 μm, a tube voltage of 60 kV and an electron beam power of 9 W [29]. The data were acquired by a CMOS flat panel with a replaceable Gadox scintillator, containing 512 by 1024 pixels at a pixel size of 48 μm. Because of the relatively small difference in the attenuation coefficient between water and the fibers, iodine was added to the water (0.97 mol/l) to increase its attenuation coefficient. This resulted in reconstructed cross-sections showing void areas, representing the fiber material.

To evaluate the effect of the packing density on the diffusion properties experimentally, 54 straight fiber bundles with varying FD were fabricated by holding a varying number of fiber filaments together in a shrinking tube with an inside diameter of 9.5 mm. The fiber phantoms were fixed to a PMMA plate and placed in a cylindrical container. The fiber phantoms were oriented parallel to B_0 to eliminate magnetic field gradients induced through local susceptibility differences and their effect on the diffusion measurement [5,30].

3.2.2. MR imaging measurements

Different measurements were performed at 20 °C on a Siemens Trio scanner (3T, Erlangen, Germany) equipped with an 8-element head coil:

- Diffusion weighted imaging was performed in 60 directions with an echo-planar spin echo sequence with a receiver band width (BW) of 1275 Hz/pixel. A total of 20 slices was acquired in a repetition time (TR) of 8 s and with an effective echo time (TE) of 93 ms. To minimize the influence of eddy currents, a twice-refocused spin echo (TRSE) [31] preparation was used with b-factors of 0 and 700 s/mm² The actual diffusion time Δ was estimated to be 36 ms based on the protocol used for scanning. The resolution was 2 mm × 2 mm × 2 mm. The diffusion weighted images were used to estimate the diffusion tensors (DT) by linear regression and derive the dependency of diffusion on direction [22]. Fiber tracking was performed using an Euler line integration algorithm [32].

- Proton density measurements were performed with a multiple spin echo sequence with 32 contrasts with an inter-echo time spacing $\Delta TE = 40$ ms, a TR of 10 s and BW = 130 Hz/pixel. The resolution was 0.9 mm × 0.9 mm × 2 mm. Test tubes with varying concentrations of deuterium oxide (D_2O) were used as concentration standard. The proton density fraction was obtained by fitting S_0 and T_2 to the T_2-decay function $S(TE) = S_0 e^{-TE/T_2}$ whereby the fraction was taken of the signal S_0 in a region of interest (ROI) of the phantom over S_0 in a neighboring ROI containing water. The fiber packing density equals 1-proton density fraction.

3.2.3. NMR bulk measurements

One fiber phantom with a measured proton density of 0.45 ± 0.05 was used to determine the time-dependent apparent diffusion coefficient (D_{app}) and kurtosis (K_{app}). Quantitative diffusion measurements were performed on a 0.5 T bench top NMR relaxometer equipped with a pulsed gradient unit (Brüker Minispec mq20). Both a diffusion weighted pulsed-field gradient stimulated echo (STIM) and a spin echo (SE) sequence were applied. Various diffusion weighted gradients (0 up to 2 T/m) were applied perpendicular to the fiber directions for increasing diffusion times ($\Delta = 20$ ms up to 100 ms for STIM, $\Delta = 4$ ms up to 50 ms for SE, $\delta = 0.7$ ms). The acquired signal was averaged over 15 measurements to obtain a sufficiently high signal-to-noise ratio. To minimize the influence of field inhomogeneities and gradient imperfections on the result-

ing b-factors, a calibration was performed on a water sample with dimensions similar to the fiber phantom. The temperature was kept constant at 40 °C ($D_{free} = 3.28 \times 10^{-3}$ mm^2/s [2]). The difference in radius between 20 and 40 °C was immeasurably small. $D_{app}(\Delta)$ and $K_{app}(\Delta)$ were obtained by fitting the $\ln\left(\frac{S(b)}{S(b=0)}\right)$-curve to Eq. (3) using a Levenberg–Marquardt algorithm.

4. Results

4.1. Monte Carlo simulations

Fig. 3 shows D_{app} obtained from the MC-simulations in the x-direction (perpendicular to the cylinder direction) for a hexagonal (Fig. 3a), square (Fig. 3b) and random packing (Fig. 3c) as a function of l_d and FD. When neglecting the statistical variation in D_{app} due to noise, D_{app} was found to be identical in both the x- and the y-direction. D_{app} in the z-direction (along the cylinder) for the hexagonal packing arrangement is shown in Fig. 3d. In this direction D_{app} equals the diffusion coefficient of a free medium and is independent from diffusion time or packing density. D_{appZ} was also found to be equal to D_{free} for all other packing geometries. The results for the random packing geometries with a fixed diameter were similar to the results for a random packing with a variable diameter. The precision of the simulations was 0.5%.

The Monte Carlo simulations for the diffusion in the transverse plane (x, y) reveal a short-time diffusion limit with a time-dependent D_{app} and a long-time diffusion limit
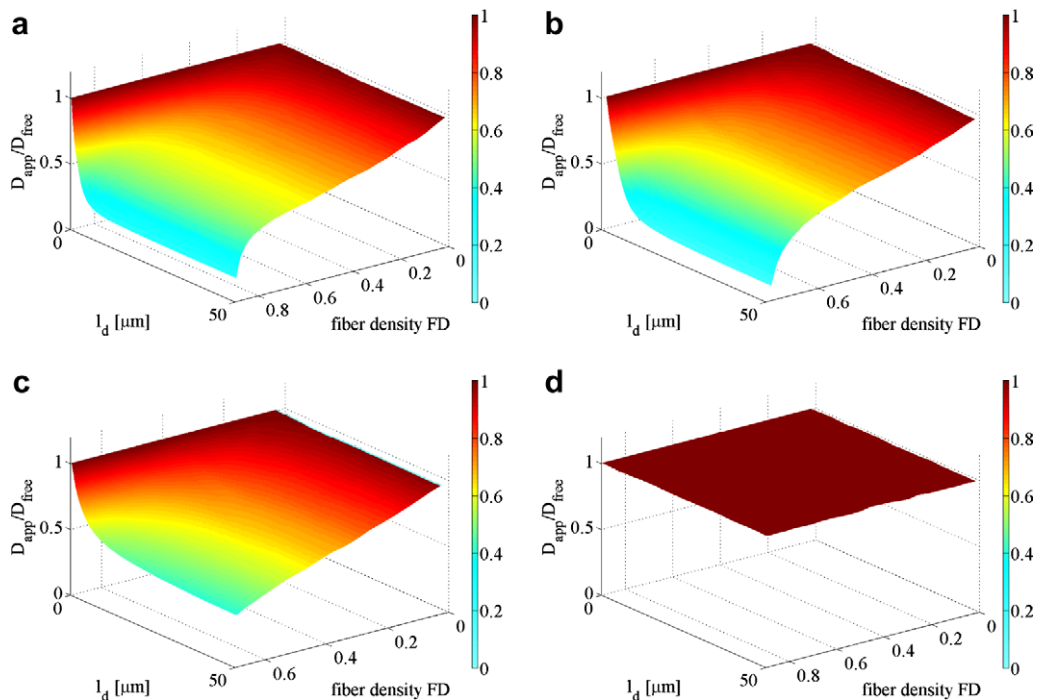

Fig. 3. Result of the Monte Carlo simulation of the diffusivities as a function of l_d and FD. D_{appX}, i.e., the diffusivity in the transverse plane is plotted for a hexagonal (a), square (b) and random (c) packing geometry. D_{appZ}, i. e. the diffusivity in the longitudinal direction, is similar for the three tested packing densities and shown for a hexagonal fiber geometry (d).

with a constant D_{app}, described by the tortuosity (Eq. (5)). As an example, Fig. 4 shows the time-decay of D_{app} as a function of l_d for the three tested packing geometries with a given density of 0.58. The decay of D_{app} in the short-time limit is the same for the three types of packing geometries with the same density and corresponds to Eq. (4) with $\frac{S}{V} = \frac{2}{R} \frac{FD}{1-FD}$ ($R = 10$ μm and FD = 0.58). However the D_{app}-decay curves deviate in the long-time diffusion limit for each geometry and fiber density.

Eq. (6) was fitted to the simulation results using a Levenberg–Marquardt algorithm to obtain D_{app} in the long-time diffusion limit (Fig. 5a) $\frac{1}{\lambda}$ and the Padé length $\sqrt{D_{free}\theta}$ (Fig. 5b). The goodness of the fit was evaluated visually and by calculating the correlation coefficient R^2. A good correspondence with the Padé interpolation Eq. (6) was obtained for the random geometries ($R^2 \geqslant 0.995$), for the hexagonal packing geometries with $0.2 \leqslant FD \leqslant 0.88$ ($R^2 \geqslant 0.992$) and for the square packing geometries with $0.2 \leqslant FD \leqslant 0.7$ ($R^2 \geqslant 0.993$). For very low fiber densities ($\leqslant 0.2$), R^2 is lower due to statistical variation caused by noise. For higher fiber densities D_{app} started to deviate systematically from Eq. (6) with increasing fiber density and tortuosity λ, resulting in the worst fit, i.e., an overestimation of the Padé length, at the highest

packing geometries ($R^2 = 0.985$ for FD = 0.78 for the square geometry and $R^2 = 0.98$ for FD = 0.78). D_{app} becomes $\frac{1}{\lambda}$ in the long-time limit. The simulation results for the regular packing geometries (Fig. 5a) confirm the theoretical predictions made in [18]. The fitted Padé lengths in Fig. 5b are about 5 μm larger for a random packing than an ordered packing geometry, which indicates a longer transition between short- and long-time limit for a random packing than for an ordered packing.

Fig. 6 shows K_{app} obtained from Monte Carlo simulations in the x-direction for a hexagonal (Fig. 6a), square (Fig. 6b) and random packing (Fig. 6c) as a function of l_d and FD. The K_{app}-curves showed the same behavior in the x- and the y-direction. The plot of K_{app} in the z-direction is similar for the three different packing geometries and is shown in Fig. 6d. The precision of the simulations was 2%.

Whereas the diffusion kurtosis reaches zero in the longitudinal direction and for long diffusion lengths in the transverse plane, the kurtosis becomes positive in the transverse plane at intermediate diffusion lengths, indicating a diffusion profile less sharply peaked than a Gaussian diffusion profile. For low fiber densities, K_{app} increases slightly with fiber density and is similar for the three packing geometries, while K_{app} increases considerably for higher fiber densities, whereby the square packing geometry results in the highest kurtosis values. It is also noted that K_{app} stays positive for longer diffusion lengths in the random than in the ordered packing geometries.

4.2. Experiments

Fig. 7a and b show a cross section and the three-dimensional reconstruction of the micro-CT scans, showing a random packing of the fibers inside the fiber phantom and a parallel alignment of the fibers in the longitudinal direction. No significant air bubble artifacts were found on the DW EPI images of the fiber bundles.

A fiber tracking example of fiber phantom is shown in Fig. 8, demonstrating a good agreement between the actual fiber direction and the direction of the reconstructed fibers.
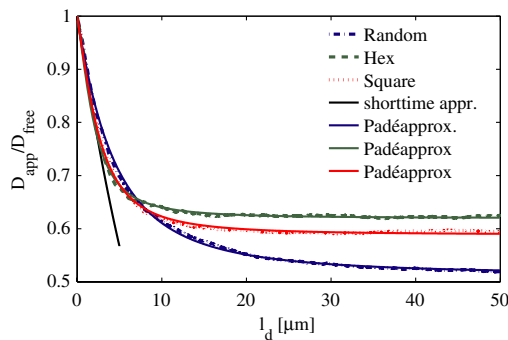

Fig. 4. Time-decay of D_{appX} in the transverse plane as a function of the l_d for the three tested fiber geometry with a given fiber density of 0.58. The short-time diffusion limit (Eq. (4)) is shown and the Padé-approximation for intermediate diffusion times (Eq. (6)) is fitted through the simulation results.
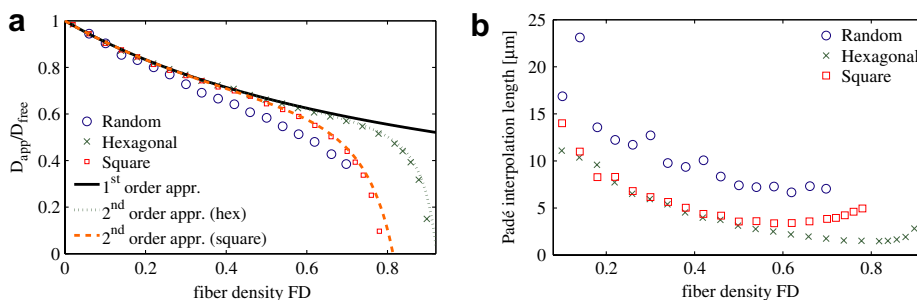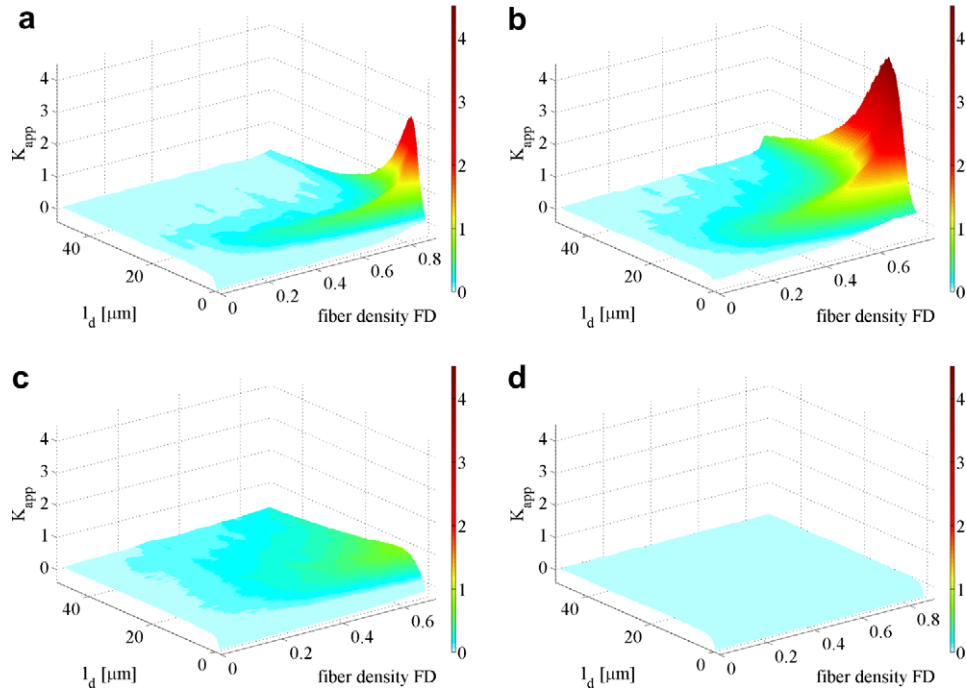

Fig. 5. Fitting results of the Padé-approximation (Eq. (6)) applied to the simulated D_{app} in the transverse plane (an average is taken of D_{appX} and D_{appY}) (a) D_{app} in the long-time limit plotted as a function of FD and compared to the Maxwell–Garnett equations of the 1st and 2nd order for a hexagonal and square packing geometry [18]. (b) The Padé length, $\sqrt{D_{free}\theta}$.

Fig. 6. Result of the Monte Carlo simulation of the kurtosis as a function of l_d and FD. K_{appX}, i.e., the kurtosis in the transverse plane is plotted for a hexagonal (a), square (b) and random (c) geometry. K_{appZ}, i.e., the kurtosis in the longitudinal direction, is similar for the three tested packing geometries and is shown for a hexagonal fiber geometry (d).
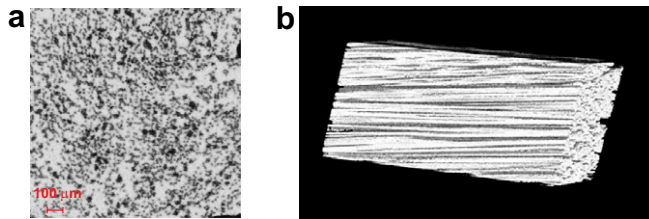

Fig. 7. (a) Micro-CT image of a cross section of a fiber phantom. (b) Three-dimensional reconstruction of a ROI chosen within the fiber phantom, note that here the void area representing the fibers is rendered opaque (white), while the iodine-doped water is rendered transparent.

Fig. 9. Comparison between the FA-measurements of the fiber phantoms and the simulated FA-values for a random and a hexagonal packing with a $\Delta = 36$ ms. This diffusion time corresponds with the long-time diffusion limit in case of a hexagonal geometry but not in case of a random geometry which is also plotted for illustration.
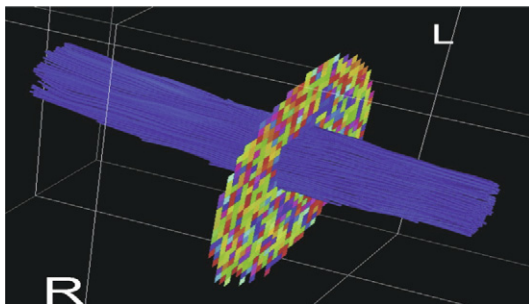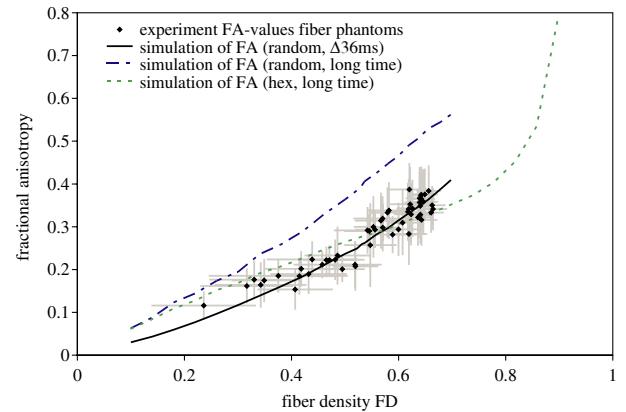

Fig. 8. Fiber tracts after DTI of a fiber phantom.

Fig. 9 shows the measured FA-values as a function of the measured FD-values. The error bars of the experimental data show the standard deviation over the chosen ROI's within the fiber phantoms (containing 297 ± 45 voxels for

the FD-measurements and 96 ± 41 voxels for the FA-measurements). The T_2-fits were performed using a Levenberg–Marquardt algorithm with all correlation coefficients $\geqslant 0.997$. The standard deviation of the FD increases with FD.

The measured FA-values can be compared with the simulated FA-values with a diffusion time according to the experimental set-up, $\Delta = 36$ ms, for a random and a hexagonal packing geometry. The best correspondence between experiment and simulations is found for a random packing geometry. As an illustration of the time-dependency, the
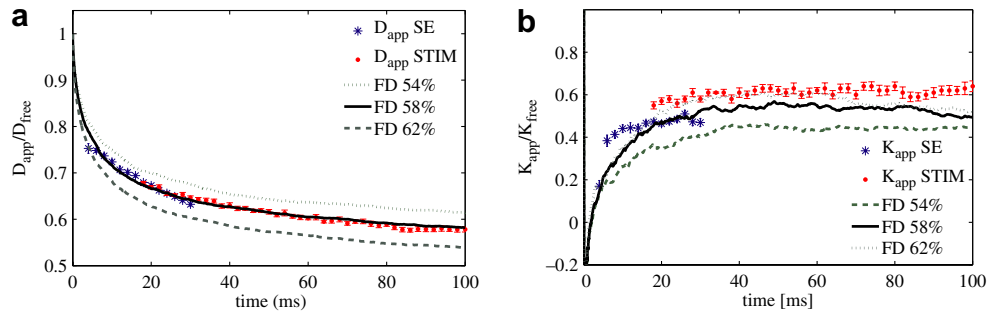
Fig. 10. Comparison between the measured diffusion parameters of a fiber phantom with FD = 0.55 ± 0.05 and simulation results for a random packing with FD = 0.54, 0.58 and 0.62. (a) $D_{app}(\Delta)$ (b) $K_{app}(\Delta)$.

simulated FA-values in the long-time diffusion limit are also shown in Fig. 9. For $\Delta = 36$ ms the long-time diffusion limit is already reached in case of the hexagonal packing geometry but not for the random packing geometry.

Fig. 10a shows the measured $D_{app}(\Delta)$ of the bulk NMR measurement of a fiber phantom in comparison with the simulated $D_{app}(\Delta)$ for a random packing with densities of 0.54, 0.58 and 0.62. The same comparison between experiment and simulation is shown for $K_{app}(\Delta)$ in Fig. 10b. The D_{app}- and K_{app}-values were fitted using a Levenberg–Marquardt algorithm with all correlation coefficients $\geqslant 0.998$. The noise level could be neglected. Taking into account the error bars, indicating the 95% confidence bounds of the fit, the fitted D_{app}-values are the same for the SE and STIM sequence, whereas for the fitting results of K_{app}, there is a difference of 10%. There is a good agreement between the experimental measured $D_{app}(\Delta)$ and the simulated $D_{app}(\Delta)$ with FD = 0.58, which matches the measured proton density fraction of the fiber phantom of 0.45 ± 0.05. However, a difference of maximum 15% was found between the simulated $K_{app}(\Delta)$ with FD = 0.58 and the experimentally measured curve.

5. Discussion

5.1. Monte Carlo simulations

The diffusion in the interstitial space between fibers was modeled in the short- and long-time limit using Monte Carlo simulations to investigate the influence of the fiber density and the packing geometry. The simulated time-dependent diffusion coefficients were verified with the theory of diffusion in porous media for the short-time (Eq. (4)) (see Fig. 4) and for the long-time diffusion limit. The simulated diffusion coefficient corresponds very well with the analytical equations derived in [18] for a hexagonal and a square packing (see Fig. 5). In contrast to the results for ordered packing arrangements, the simulations in the random packing geometries revealed higher tortuosity and anisotropy values, especially at lower fiber densities. This may be attributed to the fact that for random geometries there is a larger variation in the distance between fibers. In case of nearly touching fibers, pockets

or lakes are created in which the approaching particles get trapped, resulting in an effective diffusion coefficient of zero in the long time. This so called "pocket-effect" [33,34] also explains the differences in tortuosity between hexagonal and square packings for higher densities, where the diffusion process is mainly dominated by the pore structure of the interstitial space [35,36]. As proven by the simulation, the large spread in inter-fiber distance in a random packing geometry results in a longer transition in time between short and long-time diffusion limit in comparison with ordered geometries. As in DTI the diffusion time is typically 50 ms or more, this effect, in combination with the fiber sizes of the diffusion phantom and l_d, can not be neglected when performing quantitative DW-MRI, as shown in Fig. 9.

The simulation results were used to test the accuracy of the Padé approximation for increasing fiber densities. The Padé form of $D_{app}(\Delta)$ in Eq. (6) is an interpolation formula that connects the analytical short- and long-time diffusion limits. The physical interpretation of the Padé length $\sqrt{D_{free}\theta}$ is not straightforward since there exist different length scales in the packing geometries. Many experimental studies show that the Padé equation Eq. (6) adequately fits most 3D data such as random bead packs [12,13] and porous rocks [15]. The simulation data in this study confirm that this equation is also appropriate for fitting 2D geometries but some deviations are found for the ordered packing geometries with the highest densities. The Padé approximation seemed less suitable in the cases of 2D geometries with very high densities. Besides the Padé approximant, the time dependence of diffusion weighted MR signals can also be parametrized with an anomalous diffusion model like described in [37], where a simple model for anomalous diffusion in random disordered media and fractal spaces was used.

Monte Carlo simulations are frequently used to model the diffusion coefficient. In addition, this paper shows its utility for modeling the diffusion kurtosis, though some noise-related statistical variation is still present. The diffusion kurtosis reaches zero for long diffusion lengths in the transverse plane, confirming the supposition of a Gaussian diffusion profile that can be described by the tortuosity. However, for intermediate diffusion lengths the diffusion

kurtosis becomes positive. As the considered porous medium can be regarded as a single compartment system, K_{app} reveals here the non-Gaussian diffusion behavior caused by the presence of barriers. As shown in Fig. 6, the diffusion kurtosis increases considerably with fiber density so that the DW-MRI signal shows a non-exponential decay when b-values become large.

The simulations performed for this study and the described phantom relate to the extracellular space between the axons in brain white matter [19]. The results described here provide complementary information to the numerous *in vivo* diffusion models, such as the difference in diffusion behavior between random and ordered packing geometries and the presence of the diffusion kurtosis, resulting in a non-exponential DW-MRI signal decay for high b-values. In addition to the model for restricted diffusion described in [38], this study presents the non-Gaussian diffusion in case of hindered diffusion in the interstitial space. The question raises whether the assumption made in some diffusion models [27] is correct that the signal attenuation at high b-values is caused exclusively by diffusion in the intra-axonal space. Although the Monte Carlo simulations performed here suggest that hindered diffusion also exhibits non-Gaussian diffusive motion, the findings of this study can not been extrapolated directly to the case of diffusion in the extra-axonal space. The geometry of brain white matter differs from the model of packed cylinders used in this study. The diameter of the cylinders used in the simulations was in average 20 μm and the maximum fiber packing density for a random packing geometry in this study was 0.7. The diameter of the axons in brain white matter is much smaller than 20 μm [39] and the axon density is measured to be about 0.8 [40]. Both differences can diminish or shorten the effect of kurtosis in the diffusion measurements.

In order to test the several diffusion models described in the literature, it would be interesting to create more realistic phantoms such as capillaries, imitating the diffusion in both intracellular and extracellular space of brain white matter.

5.2. Experiments

Fig. 9 demonstrates a good agreement between the experimentally derived FA in the fiber phantoms and the corresponding simulated FA for random cylinder packing geometries with the corresponding densities. Moreover, the time-dependent D_{app} and K_{app} demonstrate the best agreement with the corresponding fiber density for a random packing geometry as can be seen from Fig. 10. By performing the measurement at 40 °C, the term $(bD_{free})^2$ in Eq. (3) was high enough for the signal decay to become non-exponential and K_{app} could be fitted. The small differences between the measured K_{app} with the SE and the STIM sequence can be explained by the slightly different range of b-values used in both experiments. The data obtained with the bulk NMR experiments are not precise enough

to resolve the higher order coefficients (kurtosis, . . .). However, incorporation of a higher order terms in the fitting of $\ln(S)$ turned out to be necessary to obtain an accurate description of D_{app} [41].

The hypothesis of a random packing geometry is verified in Fig. 7. The random geometry is a consequence of the fabrication method of the fiber phantoms which does not allow for controlling the distance between the fibers. Although in reality the fibers are not perfectly parallel, the effect of the variation in the longitudinal directions is negligible in comparison with the effect of the packing arrangement in the transverse plane. Thus, the model of parallel aligned cylinders is suitable for modeling the diffusion in the fiber phantom.

Thanks to the shrinking tubes, the fiber phantoms could be manufactured in a reproducible way. The homogeneity of the fiber density increased with fiber density, indicating that for low FD, the Dyneema® fibers tend to cluster together in the middle of the shrinking tube of the fiber phantom (also visible in the micro-CT image Fig. 7). Possible deviations in the coregistration between the proton density and FA-images due to the difference in resolution, may have caused a slight overestimation of FA for the low fiber densities. Since the effect of clustering of the fibers within the selected voxels would result in a decrease of FA (simulation data not shown here), the assumption that the fibers are homogeneously random packed within the size of the voxels seems valid.

As the diffusion is restricted to the interstitial space between the hydrophobic fibers, the proton density is lower in comparison with that measured in *in vivo* DW-MRI experiments of the brain, where the myelinated axons have a tubular structure. However, for the preparation of the fiber phantoms, non-doped water is used, so the large T_1 and T_2 relaxation times compensated for the signal loss in proton density, resulting in a high signal-to-noise ratio. In this study, possible effects of local susceptibility differences on the diffusion measurement were eliminated by orienting the fibers parallel to B_0. This problem is to be addressed in the future. The effect of surface relaxation in the short-time [24] and long-time [42] has been described in the literature. Preliminary measurements and simulations of the surface relaxation and its effect on the apparent diffusion coefficient have been carried out to conclude that the effect can be neglected in this study.

Several possible applications for Dyneema® fiber phantoms can be pointed out. As they have a well-known diffusion behaviour, they can serve as a reference tool. In this way, they can be applied to provide a daily reproducible standard for DTI and to set systematic error limits on FA and other diffusion parameters. They are also helpful in multi-center studies. The FA-values were high enough to perform fiber tracking and the obtained fiber tracts correspond with reality which makes these fiber phantoms helpful for testing tractography algorithms. The flexibility of the shrinking tubes enables the construction of fiber tract topologies.

6. Conclusion

The diffusion in the interstitial space of an anisotropic fiber phantom was measured using DW-MRI and bulk NMR measurements. The measured diffusion parameters agree with those obtained through Monte Carlo simulations of diffusion in porous media consisting of parallel randomly packed cylinders. The MC simulations confirm the accuracy and validity of the existing analytical models for ordered packing geometries. The simulations in the random geometries revealed higher anisotropy values and a longer transition between the short and long-time diffusion limit in comparison with ordered packing geometries.

From this work, we can conclude that Dyneema® fiber phantoms are appropriate for testing DW-MRI sequences and diffusion parameters on clinical MRI-scanners quantitatively.

References

[1] D. Le Bihan, Looking into the functional architecture of the brain with diffusion MRI, Nat. Rev. Neurosci. 4 (6) (2003) 469–480.

[2] P.S. Tofts, D. Lloyd, C.A. Clark, G.J. Barker, G.J.M. Parker, P. McConville, C. Baldock, J.M. Pope, Test liquids for quantitative MRI measurements of self-diffusion coefficient in vivo, Magn. Reson. Med. 43 (3) (2000) 368–374.

[3] I. Delakis, E.M. Moore, M.O. Leach, J.P. De Wilde, Developing a quality control protocol for diffusion imaging on a clinical MRI system, Phys. Med. Biol. 49 (8) (2004) 1409–1422.

[4] B. Hills, Magnetic Resonance Imaging in Food Science, John Wiley, New York, USA, 1998.

[5] J.D. Trudeau, W.T. Dixon, J. Hawkins, The effect of inhomogeneous sample susceptibility on measured diffusion anisotropy using NMR imaging, J. Magn. Reson. B 108 (1) (1995) 22–30.

[6] S. Madi, K.M. Hasan, P.A. Narayana, Diffusion tensor imaging of in vivo and excised rat spinal cord at 7 T with an icosahedral encoding scheme, Magn. Reson. Med. 53 (1) (2005) 118–125.

[7] E.A.H. von dem Hagen, R.M. Henkelman, Orientational diffusion reflects fiber structure within a voxel, Magn. Reson. Med. 48 (3) (2002) 454–459.

[8] C.-P. Lin, V.J. Wedeen, J.-H. Chen, C. Yao, W.-Y.I. Tseng, Validation of diffusion spectrum magnetic resonance imaging with manganese-enhanced rat optic tracts and ex vivo phantoms, NeuroImage 19 (3) (2003) 482–495.

[9] N. Yanasak, J. Allison, Use of capillaries in the construction of an MRI phantom for the assessment of diffusion tensor imaging: demonstration of performance, Magn. Reson. Imaging 24 (10) (2006) 1349–1361.

[10] M. Perrin, C. Poupon, B. Rieul, P. Leroux, A. Constantinesco, J.-F. Mangin, D. Le Bihan, Validation of q-ball imaging with a diffusion fibre-crossing phantom on a clinical scanner, Philos. Trans. R. Soc. Lond. B Biol. Sci. 360 (1457) (2005) 881–891.

[11] E. Fieremans, S. Delputte, K. Deblaere, Y. De Deene, B. Truyens, Y. D'Asseler, E. Achten, I. Lemahieu, R. Van de Walle, A flexible hardware phantom for validation of diffusion imaging sequences, in: Proceedings of the ISMRM 13th scientific meeting, Miami, USA, 2005, p. 269.

[12] L.L. Latour, P.P. Mitra, R.L. Kleinberg, C.H. Sotak, Time-dependent diffusion coefficient of fluids in porous media as a probe of surface-to-volume ratio, J. Magn. Reson. Ser. A 101 (3) (1993) 342–346.

[13] R.W. Mair, P.N. Sen, M.D. Hürlimann, S. Patz, D.G. Cory, R.L. Walsworth, The narrow pulse approximation and long length scale determination in xenon gas diffusion NMR studies of model porous media, J. Magn. Reson. 156 (2) (2002) 202–212.

[14] M. Hürlimann, K. Helmer, L. Latour, C. Sotak, Restricted diffusion in sedimentary rocks. determination of surface-to-volume ratio and surface relaxivity, J. Magn. Reson. Ser. A 111 (1994) 169–178.

[15] Y.-Q. Song, Determining pore sizes using an internal magnetic field, J. Magn. Reson. 143 (2) (2000) 397–401.

[16] L.L. Latour, K. Svoboda, P.P. Mitra, C.H. Sotak, Time-dependent diffusion of water in a biological model system, Proc. Natl. Acad. Sci. USA 91 (4) (1994) 1229–1233.

[17] K.G. Helmer, B.J. Dardzinski, C.H. Sotak, The application of porous-media theory to the investigation of time-dependent diffusion in in vivo systems, NMR Biomed. 8 (7–8) (1995) 297–306.

[18] P.N. Sen, P.J. Basser, A model for diffusion in white matter in the brain, Biophys. J. 89 (5) (2005) 2927–2938.

[19] D.G. Norris, The effects of microscopic tissue parameters on the diffusion weighted magnetic resonance imaging experiment, NMR Biomed. 14 (2) (2001) 77–93.

[20] E.O. Stejskal, Use of spin echoes in a pulsed magnetic-field gradient to study anisotropic, restricted diffusion and flow, J. Chem. Phys. 43 (10) (1965) 3597–3603.

[21] J.H. Jensen, J.A. Helpern, A. Ramani, H. Lu, K. Kaczynski, Diffusional kurtosis imaging: the quantification of non-Gaussian water diffusion by means of magnetic resonance imaging, Magn. Reson. Med. 53 (6) (2005) 1432–1440.

[22] P.J. Basser, J. Mattiello, D. Le Bihan, Estimation of the effective self-diffusion tensor from the NMR spin echo, J. Magn. Reson. Ser. B 103 (3) (1994) 247–254.

[23] P.P. Mitra, P.N. Sen, L.M. Schwartz, P. Le Doussal, Diffusion propagator as a probe of the structure of porous media, Phys. Rev. Lett. 68 (24) (1992) 3555–3558.

[24] P.P. Mitra, P.N. Sen, L.M. Schwartz, Short-time behavior of the diffusion coefficient as a geometrical probe of porous media, Phys. Rev. B Cond. Matt. 47 (14) (1993) 8565–8574.

[25] W.T. Perrins, D.R. Mckenzie, R.C. Mcphedran, Transport properties of regular arrays of cylinders, Proc. R. Soc. Lond. A 369 (1979) 207–225.

[26] L.J. Zielinski, P.N. Sen, Effects of finite-width pulses in the pulsed-field gradient measurement of the diffusion coefficient in connected porous media, J. Magn. Reson. 165 (1) (2003) 153–161.

[27] Y. Assaf, R.Z. Freidlin, G.K. Rohde, P.J. Basser, New modeling and experimental framework to characterize hindered and restricted water diffusion in brain white matter, Magn. Reson. Med. 52 (5) (2004) 965–978.

[28] P.J. Basser, Inferring microstructural features and the physiological state of tissues from diffusion-weighted images, NMR Biomed. 8 (7–8) (1995) 333–344.

[29] B.C. Masschaele, V. Cnudde, M. Dierick, P. Jacobs, L. Van Hoorebeke, J. Vlassenbroeck, UGCT: new X-ray radiography and tomography facility, Nucl. Instruments Methods Phys. Res. Sect. A Accelerators Spectrometers Detectors Associated Equipment 580 (2007) 266–269.

[30] C. Beaulieu, P.S. Allen, An in vitro evaluation of the effects of local magnetic-susceptibility-induced gradients on anisotropic water diffusion in nerve, Magn. Reson. Med. 36 (1) (1996) 39–44.

[31] T.G. Reese, O. Heid, R.M. Weisskoff, V.J. Wedeen, Reduction of eddy-current-induced distortion in diffusion MRI using a twice-refocused spin echo, Magn. Reson. Med. 49 (1) (2003) 177–182.

[32] P.J. Basser, D.K. Jones, Diffusion-tensor MRI: theory, experimental design and data analysis—a technical review, NMR Biomed. 15 (2002) 456–467.

[33] C. Nicholson, Diffusion and related transport mechanisms in brain tissue, Rep. Prog. Phys. 64 (2001) 815–884.

[34] J.R. Kalnin, Calculations of the effective diffusion coefficient for inhomogeneous media, J. Phys. Chem. Sol. 63 (2002) 449–456.

[35] R.G. Thorne, C. Nicholson, In vivo diffusion analysis with quantum dots and dextrans predicts the width of brain extracellular space, PNAS 103 (14) (2006) 5567–5572.

[36] K.C. Chen, C. Nicholson, Changes in brain cell shape create residual extracellular space volume and explain tortuosity behavior during osmotic challenge, Proc. Natl. Acad. Sci. USA 97 (15) (2000) 8306–8311.

[37] E. Ozarslan, P.J. Basser, T.M. Shepherd, P.E. Thelwall, B.C. Vemuri, S.J. Blackband, Observation of anomalous diffusion in excised tissue by characterizing the diffusion-time dependence of the MR signal, J. Magn. Reson. 183 (2) (2006) 315–323.

[38] C. Liu, R. Bammer, M.E. Moseley, Limitations of apparent diffusion coefficient-based models in characterizing non-Gaussian diffusion, Magn. Reson. Med. 54 (2) (2005) 419–428.

[39] C. Beaulieu, The basis of anisotropic water diffusion in the nervous system—a technical review, NMR Biomed. 15 (7–8) (2002) 435–455.

[40] D. Le Bihan, The 'wet mind': water and functional neuroimaging, Phys. Med. Biol. 52 (7) (2007) 57–90.

[41] V.G. Kiselev, K.A. Il'yasov, Is the "biexponential diffusion" biexponential? Magn. Reson. Med. 57 (3) (2007) 464–469.

[42] P.N. Sen, L.M. Schwartz, P.P. Mitra, B.I. Halperin, Surface relaxation and the long-time diffusion coefficient in porous media: periodic geometries, Phys. Rev. B 49 (1) (1994) 215–225.